Received 23 April 2024; accepted 6 June 2024. Date of publication 12 June 2024; date of current version 21 June 2024.

Digital Object Identifier 10.1109/OJUFFC.2024.3413603

Equivalent Circuit Modeling of Air-Coupled Laterally Actuated Electrostatic Bulk-Mode MEMS

TONY MERRIEN[1], PIERRE DIDIER[2], AND EMMANUELLE ALGRÉ[1]

[1]ESYCOM Laboratory, UMR 9007 CNRS, Université Gustave Eiffel, 77454 Marne-la-Vallée, France
[2]CERTES (EA 3481), Université Paris-Est Créteil, 94010 Créteil, France

CORRESPONDING AUTHOR: T. MERRIEN (tony.merrien@esiee.fr)

ABSTRACT In this paper, a linear lumped-element equivalent circuit model (ECM) for ultrasonic laterally transduced electrostatic bulk-mode air-coupled resonant micro-electro-mechanical systems (MEMS) is described. A single-crystal silicon (SCS) square plate with T-shaped tethers is considered as the geometry of interest with a one-sided electrostatic actuation. This type of sensor can be used for sensitive mass sensing of airborne particles and possesses a large active surface with in-plane vibration modes in the ultrasonic frequency range. Firstly, the eigensolutions and eigenvectors of the problem are obtained using analytical equations and compared with finite-element modeling (FEM) solutions. Secondly, using modal analysis, the number of degrees of freedom is reduced and individual solutions are provided for each vibration mode, leading to various effective masses, stiffnesses and dampings. The first order Taylor expansion of both the electrical current equation and the electrostatic force applied on the resonator allows one to obtain expressions for the additional stiffness and the electro-mechanical transformation coefficient linked to the membrane actuation. Based on theses results, single-input single output (SISO) equivalent circuits are established using electro-mechanical and Butterworth-Van Dyke (BVD) approaches. Electrical admittance simulations resulting from different in-plane vibration modes are proven to be in excellent agreement with FEM simulations. Finally, a numerical mass sensing application is described to evaluate the relevance of both the model and the resonator design to act as a microbalance. The proposed model can be used to design, predict, analyze and optimize the behavior of highly sensitive air-coupled ultrasonic bulk-mode SCS MEMS for various physical applications.

INDEX TERMS Capacitive, FEM, microbalance, modal analysis, silicon, resonator, ultrasonic.

I. INTRODUCTION

RESONATOR sensors have been a topic of research for multiple decades now [1], [2], [3], [4], [5], [6]. With the manufacturing progresses made in the field of micro-electronics, micro-electro-mechanical systems (MEMS) have emerged as ideal sensors for various applications thanks to high levels of reproducibility, robustness and reliability [7]. In the case of resonators, the commonly employed manufacturing material is single-crystal silicon (SCS) which possesses great mechanical properties that can be used in conjunction with MEMS inherent enhanced miniaturization capabilities and a high driving electronics integration potential. From a design perspective, researchers and engineers are looking for very high quality factors (*i.e.,* low damping) to measure small variations of physical parameters (*e.g.,* temperature, pressure, gas concentration, particle presence). Our group is mainly interested in airborne aerosol particle detection for air quality monitoring using MEMS resonators as microbalances. The excitation-detection actuation mechanisms behind SCS MEMS are usually either electrostatic, piezoelectric, piezoresistive, magnetic, optic or a mix between them [8].

Most resonators can be depicted as beams or plates whose actuation occurs along the axis where the structure dimension is the smallest. This is practical because classical tools in mechanical and vibration analysis can be employed to model the membrane dynamics [9], [10]. In addition, the finite-element method (FEM) is often

employed to resolve the discretized version of the behavioral equations linked to resonators of various shapes and sizes [11]. Modeling is a key step in the framework of micro-sensors and is needed for design purposes up to electronics integration and optimization. Indeed, it is mandatory to understand the underlying physical phenomena occurring in sensors of any technology while performing measurements to ensure their functionality in the desired application field. Combining mechanics and electronics in the case of SCS MEMS, FEM tools are time consuming and a versatile reduced-order lumped-element model is generally preferable [12], [13].

In this paper, we are interested in a large freely vibrating square suspended membrane with constrained T-shaped tethers for airborne mass sensing applications [14]. The resonator is laterally excited using electrostatic forces originating from an electrode that partially covers the plate side length. This type of structure with lateral excitation is employed to favor the high-frequency sensitive in-plane longitudinal vibration modes (*e.g.,* Lamé, butterfly, extensional) of the resonator [15], [16], [17]. The resonator is defined as a single-input single-output (SISO) system using its electrostatic driving and capacitive sensing capabilities to generate and detect signals [18]. Such resonators have been previously fabricated by our group, demonstrated low anchor losses with high sensitivity and a great experimental potential for the detection of sub-ng airborne particles using in-plane vibration modes around 4 MHz [19]. Compared with other microbalances architectures in a similar frequency range [20], this setup as the advantage of having a very large active surface (*i.e.,* superior to 1 mm^2) which maximizes the detection of small-size particles [21].

Models based on transmission line theory exist for quartz crystal microbalances (QCM) that are very practical to determine physical loading media parameters variations on the membrane (*e.g.,* added mass, humidity, viscoelasticity) [22]. However, to our knowledge, lumped-element models describing the behavior of electrostatic SCS MEMS microbalances only exists in the case of disks, clamped beams or top-to-bottom actuated plates [23], [24], [25], [26], [27]. Following our previous experimental results, the aim of this paper is to establish a linear lumped-parameter equivalent circuit model (ECM) of laterally actuated electrostatic MEMS which will be used as a guiding tool for design and optimization of such microbalances. For clarity purposes, fringing field effects are neglected throughout this analysis but may affect laterally transduced electrostatic SCS MEMS depending on the plate width-to-gap ratio [28].

This paper is organized as follows: the first section is dedicated to the eigensolutions analysis of the aforementioned problem. Analytical equations are provided for the anistropic freely vibrating square membrane and compared with a FEM analysis of the geometry of interest. The second section focuses on the model setup, starting with the discretized version of the mechanical displacement equation. A modal analysis is employed to reduce the number of degrees of freedom and obtain lumped mechanical parameters. A first order Taylor expansion is employed to linearize the electrostatic force acting on the resonator as well as the current equation. Resulting equations lead to equivalent circuit representations for laterally actuated MEMS. The third section is the validation study of the lumped-element ECM developed based on electrical admittance results confrontation with FEM. The final section is a discussion surrounding the model limits and its importance in the broad landscape of existing modeling techniques for ultrasonic electrostatic MEMS. Using a numerical mass sensing application case, the relevance of the model and the resonator design are established when compared with an analytical expression analogous to the Sauerbrey equation. In addition, a first appendix provides the anisotropic silicon tensor matrix used for computations and a second provides the analytical square in-plane plate mode shapes.

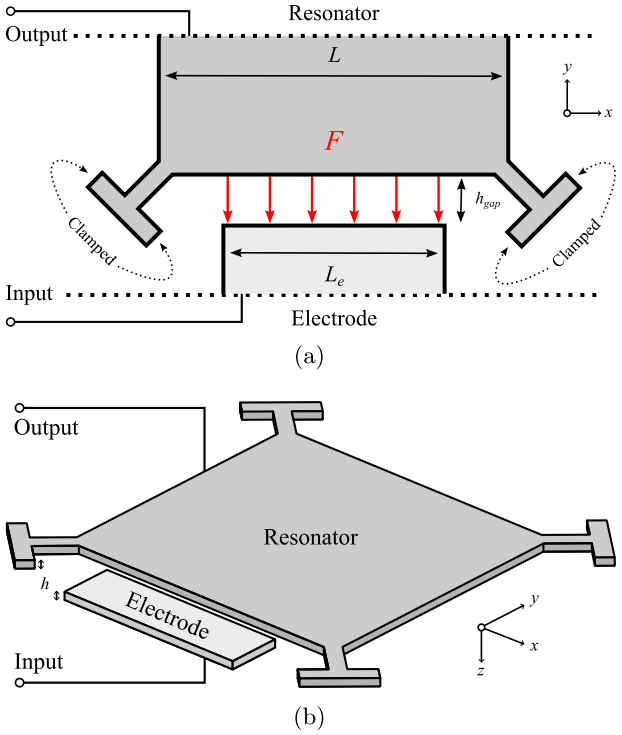

FIGURE 1. Illustration of the SISO SCS MEMS resonator (a) viewed from the top and (b) viewed from the side. The axial electrostatic force *F* acting on the membrane along the *x* axis is denoted in red.

II. IN-PLANE VIBRATION MODES

The SCS MEMS geometry is illustrated Figure 1. The actuation electrode has a length $L_e = 0.75$ mm that partially covers the square resonator of length and width $L = 1$ mm. The electrode and the resonator have a thickness of $h = 40$ μm (*i.e.,* $h \ll L_e < L$) and are both separated by a gap height of $h_{gap} = 2$ μm. The membrane is freely vibrating and only the sides of the four T-shaped tethers are constrained. The tethers are 56 μm in length and width.

TABLE 1. Comparison of the SCS plate with T-shaped tethers in-plane resonances obtained using FEM and the analytical equations (1), (2) and (3) given in the case of a freely vibrating anisotropic square plate.

Mode	Analytical	FEM	Error
Lamé (f_1)	4.1282 MHz	4.1291 MHz	0.02%
Butterfly (f_2)	4.5680 MHz	4.5524 MHz	0.34%
Extensional (f_3)	4.8956 MHz	4.6084 MHz	6.23%

A. ANALYTICAL EQUATIONS

A common approach to estimate the solutions of the eigenproblem related to MEMS mechanical structures, provided that its constitutive material properties are known, is to use analytical equations. In our case, the geometry closely resembles that of a free square membrane. As described by H. Ekstein [29], the first three bulk-mode, so-called longitudinal, resonance frequencies denoted here f_1, f_2 and f_3 (*i.e.,* the Lamé, butterfly and extensional modes, respectively) of a freely vibrating anisotropic square plate are equal to

$$f_1 = \frac{1}{2L}\sqrt{\frac{(C_{11}-C_{12})}{\rho}}\,, \tag{1}$$

$$f_2 = \frac{1}{2L}\sqrt{\frac{C_{11}}{\rho}}\,, \tag{2}$$

$$f_3 = \frac{1}{2L}\sqrt{\frac{C_{11}}{\rho}+\frac{8}{\pi^2}\frac{C_{12}}{\rho}}\,, \tag{3}$$

where C_{ij} are coefficients of the silicon tensor matrix that intrinsically depend on the silicon crystal orientation and ρ is the plate density.

In this work, the silicon (100) wafer is considered to be aligned in the ⟨110⟩ crystal directions. In addition, the silicon is assumed orthotropic (*i.e.,* possesses two orthogonal planes of symmetry) and the stiffness coefficients can thus be expressed using the material's Young modulus and Poisson coefficient in each direction, as described in details by Hopcroft et al. [30]. For clarity purposes, the tensor matrix coefficients computation is reported in the appendix A of this work. The plate's properties employed are equal to

$$C_{11} = 194.5 \text{ GPa}\,, \tag{4}$$

$$C_{12} = 35.7 \text{ GPa}\,, \tag{5}$$

$$\rho = 2330 \text{ kg/m}^3. \tag{6}$$

The analytical equations results for the bulk-mode resonance frequencies in accordance with the presented sensor geometry and properties are reported in the Table 1.

B. FINITE-ELEMENT ANALYSIS

To evaluate the accuracy of the analytical equations with regards to the considered geometry and determine the tethers influence, a FEM analysis is performed using COMSOL Multiphysics™ v6.1 (COMSOL AB, Stockholm, Sweden)

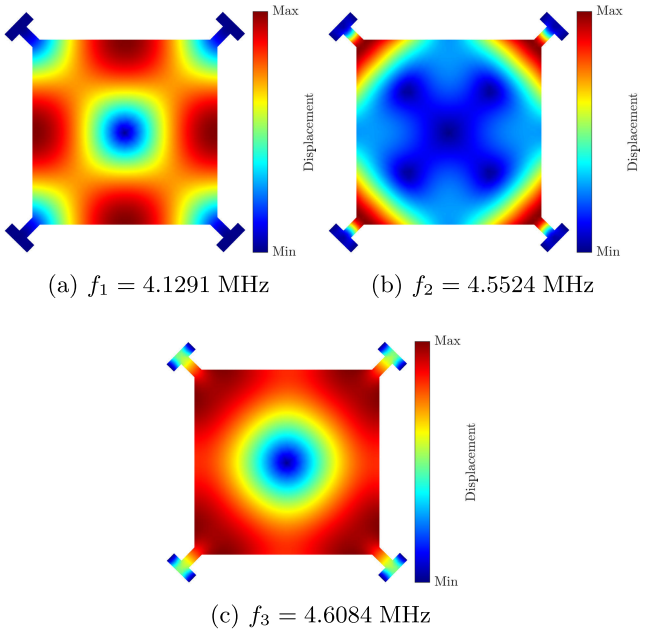

(a) $f_1 = 4.1291$ MHz (b) $f_2 = 4.5524$ MHz

(c) $f_3 = 4.6084$ MHz

FIGURE 2. Anisotropic silicon plate eigenfrequencies and mode shapes magnitude obtained using FEM where (a) is the Lamé mode, (b) is the butterfly mode and (c) is the extensional mode.

and results are presented Figure 2. The eigenfrequencies obtained are reported in Table 1 for comparison purposes.

It is interesting to note that, even with tethers, the considered geometry displays similar in-plane plate mode shapes as expected in the case of a perfectly square membrane. This result is practical because it means that the classical analytical bulk-mode square plate mode shape equations may be considered to approximate the eigenvectors solutions of the geometry of interest. These equations, obtained by H. Ekstein [29], are reported in the appendix B of this paper. From a practical perspective, one sees that the butterfly mode has the disadvantage of having the smallest actively vibrating surface hence is less interesting to optimize particle presence detection in the case of air-coupled sensitive microbalances.

As expected when it comes to the eigensolutions, the error between the analytical equations and FEM is the highest for the extensional mode. Indeed, the T-shaped tethers at each plate corner are on a vibration node for both the Lamé and the butterfly modes but not in the case of the extensional mode. In addition, the T-shaped tethers affect the physical damping of the device differently as a function of frequency and therefore its quality factor may vary for each mode [31], [32]. More specifically, based on previous experimental and simulation results, an increase in anchor length tends to reduce the overall quality factor of the device and even more so in the case of the extensional mode [19]. Therefore, to perform accurate assessment of particle deposition on the membrane, it is ideal to evaluate the resonance and quality factor of the microbalance at different vibration modes.

III. MODEL SETUP

Throughout this paper, the notation [ ] is employed to define a matrix, { } to define a vector, ^{T} their transpose form, $\dot{}$ to define the time derivative of a variable and $\tilde{}$ to define a time independent variable amplitude.

A. MECHANICAL BEHAVORIAL EQUATION

Based on the MEMS geometry depicted Figure 1, the time dependent membrane displacement is defined using the discretized version of Newton's second law

$$[M]\frac{\partial^2\{u\}}{\partial t^2} + [R]\frac{\partial\{u\}}{\partial t} + [K]\{u\} = \{q\}\ , \tag{7}$$

where $\{u\}$ is the displacement vector, $[M]$ is the mass matrix, $[K]$ is the stiffness matrix, $[R]$ is the damping matrix and $\{q\}$ is the axial load vector acting on the membrane. In classical mechanical problems, the mass matrix is diagonal and defined using the density and geometrical properties of the structure at each mesh node. The stiffness matrix is harder to obtain as it classically relies on the computation of Laplace operators using beam or plate theory [9] and can be computed using numerical methods such as FEM [33] or finite difference [34]. In this paper, due to the non-conventional mechanical structure, boundary conditions, electrode disposition and because we are interested in parameters lumping for specific in-plane vibration modes, we chose to rely on a FEM-assisted modal analysis approach. The idea is to perform an analytical modal decomposition based on a FEM eigenstudy. This allows us to define the effective mechanical parameters of the plate using its various in-plane mode shapes.

Based on modal analysis principles (*i.e.,* the Galerkin method) [10], the displacement vector can be written as

$$\{u\} = [\phi]\{\xi\}\ , \tag{8}$$

where $[\phi] = [\{\phi_1\}, \{\phi_2\}, \ldots, \{\phi_n\}]$ are the plate mode shapes (*i.e,* the normalized eigenvectors of the undamped problem in the absence of load) and $\{\xi\} = \{\xi_1, \xi_2, \ldots, \xi_n\}$ are the time dependent modal coordinates. Writing equation (7) with the modal displacement solution at mode i yields

$$[M]\{\phi_i\}\frac{\partial^2\xi_i}{\partial t^2} + [R]\{\phi_i\}\frac{\partial\xi_i}{\partial t} + [K]\{\phi_i\}\xi_i = \{q\}. \tag{9}$$

Multiplying each side of this equation by the transposed mode shape vector allows one to define classical modal parameters. Here, the modal mass m_i, sometimes refer to as the effective mass, is defined as

$$m_i = \{\phi_i\}^T[M]\{\phi_i\} = \chi_i\rho hS\ , \tag{10}$$

where S is the resonator surface. The term χ_i can be deduced from this modal analysis and translates the effective proportion of the membrane total physical mass that actively contributes to the vibration mode. The modal stiffness is equal to

$$k_i = \{\phi_i\}^T[K]\{\phi_i\} = m_i\omega_i^2\ , \tag{11}$$

and is linked to the eigensolutions ω_i^2 of the problem

$$\omega_i^2 = (2\pi f_i)^2 = \frac{\{\phi_i\}^T[K]\{\phi_i\}}{\{\phi_i\}^T[M]\{\phi_i\}}\ , \tag{12}$$

which can be used to express the natural frequency f_i at mode i. The modal damping is equal to

$$r_i = \{\phi_i\}^T[R]\{\phi_i\} = \frac{\sqrt{m_ik_i}}{Q_i} = \alpha m_i + \beta k_i\ , \tag{13}$$

which can also be expressed using the quality factor Q_i at mode i or the Rayleigh damping coefficients where α is the mass proportional damping coefficient and β the stiffness proportional damping coefficient [35]. In addition, the generalized modal force is coherently defined as

$$F_i = \{\phi_i\}^T\{q\}. \tag{14}$$

Henceforth, equation (9) can be written using modal parameters such that

$$m_i\frac{\partial^2\xi_i}{\partial t^2} + r_i\frac{\partial\xi_i}{\partial t} + k_i\xi_i = F_i. \tag{15}$$

To further develop the equation of motion, we assume that the force possesses a time independent (*i.e.,* static) component, a time dependent (*i.e.,* dynamic) component of amplitude $\tilde{F}_i$ and is purely harmonic. From this load, the resulting modal coordinates possess a static time independent and a dynamic time dependent component of amplitude $\tilde{\xi}_i$. Therefore, the static modal coordinates and force terms vanish from equation (15) which becomes the dynamic harmonic equation of motion

$$\tilde{\xi}_i\left(-\omega^2m_i + j\omega r_i + k_i\right) = \tilde{F}_i. \tag{16}$$

To compute this equation, knowledge of the applied force is needed.

B. THE ELECTROSTATIC FORCE

In our setup, the resonator is actuated using electrostatic forces oriented towards the y axis. As stated by H. Tilmans, it is fairly accurate to assume that the membrane mode shapes (*i.e.,* the normalized eigenfunctions of the problem) are not affected by the electrostatic load [26]. In addition, because we are mainly interested by the main underlying physical phenomena behind the presented setup, we also ignore fringing field effects and we consider that the electrostatic force only applies on the resonator surface S_e directly facing the electrode [36]. The generalized modal force equation (14) becomes that of the electrostatic force provided that one only considers the mode shapes nodes affecting the gap height variation

$$F_i = \iint_{S_e}\frac{\varepsilon_0\varepsilon_r}{2}\left[\frac{V_{DC}+V_{AC}}{h_{gap}-\{O\}\{\phi_i\}\xi_i}\right]^2 dS_e\ , \tag{17}$$

where $\varepsilon_0 = 8.854\times10^{-12}$ F/m is the vacuum permittivity, ε_r the gap medium relative permittivity, V_{DC} is the bias voltage,

V_{AC} is the excitation voltage, h_{gap} is the gap height and $\{O\}$ is the aperture vector

$$\{O\} = \begin{cases} 1 & \forall \{\phi_i\} \text{ affecting the gap height} \\ 0 & \text{otherwise.} \end{cases}, \tag{18}$$

Equation (17) is difficult to compute as the modal coordinates are needed for its calculation and the latter themselves require knowledge of the electrostatic force to be resolved. To do so, we chose to employ small signal approximations meaning that the modal displacement is assumed to be much lower than the gap height (*i.e.*, $\xi_i \ll h_{gap}$) and that the excitation voltage is assumed to be much lower than the bias voltage (*i.e.*, $V_{AC} \ll V_{DC}$). Combining these assumptions with a Taylor expansion of the first order leads to the linearized expression of the harmonic electrostatic force

$$F_i = \frac{\varepsilon_0 \varepsilon_r S_e V_{DC}^2}{2h_{gap}^2} + \frac{\varepsilon_0 \varepsilon_r S_e V_{DC}}{h_{gap}^2} \tilde{V}_{AC} e^{j\omega t} + \iint_{S_e} \frac{\varepsilon_0 \varepsilon_r V_{DC}^2}{h_{gap}^3} \{O\}\{\phi_i\}\tilde{\xi}_i e^{j\omega t} dS_e. \tag{19}$$

From this equation, one identifies three terms that can be described as follows: the first term is the electrostatic force in presence of bias voltage and absence of excitation voltage. The second term is the excitation voltage combined with the electrical-to-mechanical transformation coefficient η^{em} independent from the plate vibration mode

$$\eta^{em} = \frac{\varepsilon_0 \varepsilon_r S_e V_{DC}}{h_{gap}^2}. \tag{20}$$

The third term is the additional stiffness $k_{e,i}$ originating from the electrostatic pressure combined with the dynamic membrane displacement where

$$k_{e,i} = \frac{\varepsilon_0 \varepsilon_r V_{DC}^2}{h_{gap}^3} \iint_{S_e} \{O\}\{\phi_i\} dS_e = \frac{\varepsilon_0 \varepsilon_r S_e V_{DC}^2}{h_{gap}^3} \Lambda_i. \tag{21}$$

with the average modal electrostatic coefficient Λ_i equal to

$$\Lambda_i = \frac{1}{S_e} \iint_{S_e} \{O\}\{\phi_i\} dS_e. \tag{22}$$

The additional stiffness, sometimes referred to as the spring softening stiffness, lowers the resonance frequency as the bias voltage increases (cf. next section). Hence, the harmonic dynamic electrostatic force yields

$$\tilde{F}_i = \eta^{em} \tilde{V}_{AC} + k_{e,i} \tilde{\xi}_i \,, \tag{23}$$

and combining equations (23) and (16) yields the dynamic harmonic modal amplitude of the membrane

$$\tilde{\xi}_i = \frac{\eta^{em} \tilde{V}_{AC}}{-\omega^2 m_i + j\omega r_i + k_i - k_{e,i}}. \tag{24}$$

To complete this analysis, knowledge of the electric phenomena related to the mechanical behavior of the resonator are needed.

C. THE ELECTRICAL CURRENT

On the electrical side, the electrical charge is equal to the product of the capacitance C_i at vibration mode i with the voltage, classically referred to as

$$C_i V = \iint_{S_e} \frac{\varepsilon_0 \varepsilon_r (V_{DC} + V_{AC})}{h_{gap} - \{O\}\{\phi_i\}\xi_i} dS_e. \tag{25}$$

Following the same assumptions used in the linearization process of the electrostatic force, we calculate the first order Taylor expansion of the electrical charge

$$C_i V = \frac{\varepsilon_0 \varepsilon_r S_e V_{DC}}{h_{gap}} + \frac{\varepsilon_0 \varepsilon_r S_e}{h_{gap}} V_{AC} + \iint_{S_e} \frac{\varepsilon_0 \varepsilon_r V_{DC}}{h_{gap}^2} \{O\}\{\phi_i\}\xi_i dS_e. \tag{26}$$

Under harmonic consideration, the electrical current is written

$$\tilde{I}_i e^{j\omega t} = \frac{\partial C_i V}{\partial t} = j\omega \frac{\varepsilon_0 \varepsilon_r S_e}{h_{gap}} \tilde{V}_{AC} e^{j\omega t} + j\omega \iint_{S_e} \frac{\varepsilon_0 \varepsilon_r V_{DC}}{h_{gap}^2} \{O\}\{\phi_i\}\tilde{\xi}_i e^{j\omega t} dS_e \,, \tag{27}$$

where two terms can be identified: the left-hand side term is the combination of the static capacitance C_0 with the excitation voltage where

$$C_0 = \frac{\varepsilon_0 \varepsilon_r S_e}{h_{gap}} \,, \tag{28}$$

and the right-hand side term is the mechanical-to-electrical transformation coefficient η_i^{me} equal to

$$\eta_i^{me} = \frac{\varepsilon_0 \varepsilon_r V_{DC}}{h_{gap}^2} \iint_{S_e} \{O\}\{\phi_i\} dS_e = \frac{\varepsilon_0 \varepsilon_r S_e V_{DC}}{h_{gap}^2} \Lambda_i. \tag{29}$$

Note that the static capacitance is independent from the bias voltage and the plates mode shapes using the small-signal assumption.

The electrical current equation (27) now yields

$$\tilde{I}_i = j\omega(C_0 \tilde{V}_{AC} + \eta_i^{me} \tilde{\xi}_i). \tag{30}$$

This result can be viewed as the summation of two current paths, one towards the electrical capacitance of the device, the other towards its motionnal mechanical branch. Combining equations (30) with (24) and referring to the modal superposition principle, to generalized expression $\tilde{I}$ for the electrical current yields

$$\tilde{I} = \sum_{i=0}^{n} \tilde{I}_i = j\omega C_0 \tilde{V}_{AC} + \sum_{i=0}^{n} \frac{j\omega \eta_i^2 \tilde{V}_{AC}}{-\omega^2 m_i + j\omega r_i + k_i - k_{e,i}}. \tag{31}$$

where η_i^2 is defined for clarity purposes as the combination of the electro-mechanical transformation coefficients depicted

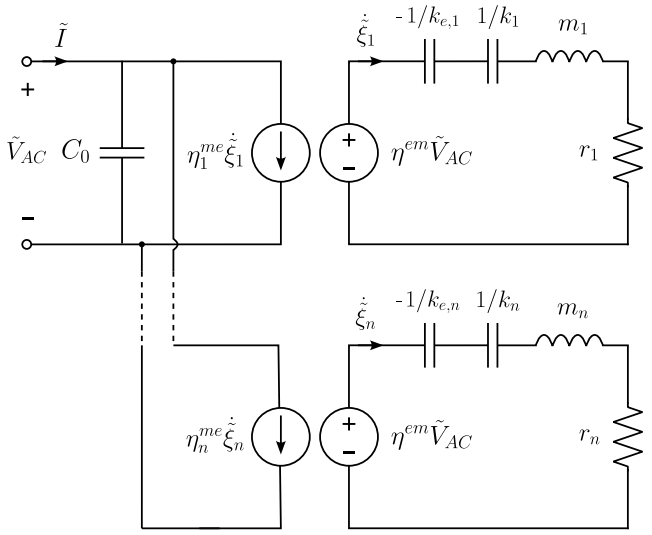

FIGURE 3. Small-signal electro-mechanical equivalent circuit model of the bulk-mode MEMS resonator. Each branch is associated with a specific in-plane vibration mode and specific effective lumped-parameters.

in equations (20) and (29) such that

$$\eta_i^2 = \eta^{em}\eta_i^{me} = \Lambda_i\left(\frac{\varepsilon_0\varepsilon_r S_e V_{DC}}{h_{gap}^2}\right)^2. \tag{32}$$

Now that all intrinsic terms of the resonators have been defined, one can deduce various equivalent circuit representations depicting its electro-mechanical behavior.

D. EQUIVALENT CIRCUIT REPRESENTATIONS

For clarity purposes in this section, we define the harmonic time derivative of the modal coordinates from equation (24), a term analogous to the membrane velocity, such that

$$\dot{\tilde{\xi}}_i = j\omega\tilde{\xi}_i = \frac{\eta^{em}\tilde{V}_{AC}}{j\omega m_i + r_i + (k_i - k_{e,i})/(j\omega)}. \tag{33}$$

The small-signal linear electro-mechanical equivalent circuit representation of the MEMS resonator is presented Figure 3.

On the electrical side, one finds the applied harmonic excitation voltage $\tilde{V}_{AC}$, the total harmonic input current $\tilde{I}$ and the static capacitance C_0 independent from the applied voltage. Based on equation (31), one sees n branches that all possess a current generator $\eta_i^{me}\dot{\tilde{\xi}}_i$ associated with the mechanical behavior of the resonator at each specific vibration mode i. On the mechanical side, each branch possesses a force generator $\eta^{em}\tilde{V}_{AC}$, a modal velocity term $\dot{\tilde{\xi}}_i$, an effective mass m_i, a damper r_i, an effective compliance $1/k_i$ and an additional compliance linked to the electrostatic load $-1/k_{e,i}$. Similar representations have been previously employed for capacitive MEMS devices and fully capture their electro-mechanical behavior based on modal decomposition principles [37], [38]. By extension, it is often more convenient to use a Butterworth-Van Dyke (BVD) representation of resonator sensors based on electrical parameters

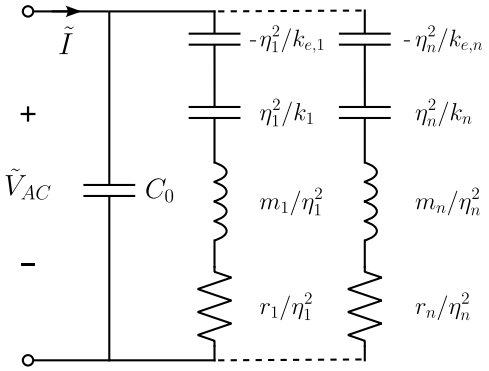

FIGURE 4. Butterworth-Van Dyke (BVD) equivalent circuit model of the bulk-mode MEMS resonator. Each branch is associated with a specific in-plane vibration mode and specific effective lumped-parameters.

only. Using the electro-mechanical transformation coefficient equation (32), one can define the entire equivalent circuit purely on the electrical side using a classical BVD representation, as presented Figure 4.

In this purely electrical representation, the negative compliance coherently becomes a negative capacitance whose physical interpretation is that the stiffness of the resonator gets smaller as the bias voltage increases [27]. Additionally, one may assume that the additional stiffness linked to the electrostatic load changes the resonance f_i by a term $\delta f_{e,i}$ such that [23]

$$f_i + \delta f_{e,i} = \frac{1}{2\pi}\sqrt{\frac{k_i - k_{e,i}}{m_i}} = f_i\sqrt{1 - \frac{k_{e,i}}{k_i}}. \tag{34}$$

In our case, the electrode active surface is very small compared to the overall resonator surface (*i.e.*, $S_e \ll S$). Therefore, it is coherent to state that the additional stiffness is very small compared to the effective stiffness (*i.e.*, $k_{e,i} \ll k_i$). This consideration leads to the resonance variation associated with the softening phenomenon being very small compared to the resonance itself (*i.e.*, $\delta f_{e,i} \ll f_i$). Using these assumptions with a first order Taylor expansion of expression (34), one finds

$$\delta f_{e,i} = -\frac{k_{e,i}}{4\pi\omega_i m_i} = -\frac{k_{e,i}}{4\pi\sqrt{k_i m_i}}. \tag{35}$$

Note that a similar theoretical analysis is often performed to evaluate small mass deposition on microbalances (*i.e.*, the small-load approximation [22], [39]), as discussed section V-B of this paper.

IV. COMPARISON WITH FEM RESULTS

To compare the results between models, we set throughout this section the Rayleigh damping coefficients to be $\alpha = 10^3\ \mathrm{s}^{-1}$ and $\beta = 10^{-12}$ s, values based on the quality factors obtained in our experimental results [19]. Indeed, the quality factors are calculated using the damping ratio expression and

TABLE 2. Parameter values independent from the bias voltage associated with the lumped-element equivalent circuit of the bulk-mode MEMS resonator for different vibration modes. Note that the quality factors, hence the modal damping coefficients, were obtained using the arbitrarily fixed Rayleigh damping coefficients $\alpha = 10^3\ \mathrm{s}^{-1}$ and $\beta = 10^{-12}$ s.

Parameter	Lamé Mode	Butterfly Mode	Extensional Mode
Modal Stiffness (k_i)	32.33 N/μm	20.26 N/μm	71.94 N/μm
Modal Mass (m_i)	48.03 μg	24.76 μg	85.80 μg
Modal Mass Factor (χ_i)	0.4876	0.2514	0.8711
Modal Damping Coefficient (r_i)	80.36×10^{-6}	45.01×10^{-6}	157.74×10^{-6}
Electrostatic Coefficient (Λ_i)	0.61	4.0×10^{-4}	0.87
Quality Factor (Q_i)	15507	15730	15748

the eigensolutions of the problem such that

$$Q_i = \frac{\omega_i}{\alpha + \omega_i^2 \beta}. \tag{36}$$

To be rigorous, Rayleigh damping coefficients ought to be evaluated experimentally or by considering every physical damping mechanisms (*e.g.,* viscous losses, anchor losses, material losses). Moreover, the gap is filled with air and we set $\varepsilon_r = 1.0006$. We denote the conductance (*i.e.,* the real part of the electrical admittance) as G and the susceptance (*i.e.,* the imaginary part of the electrical admittance) as B. Based on equation (31), the electrical admittance of the system is defined as

$$\begin{aligned} Y_{elec} &= j\omega C_0 + \sum_{i=0}^{n} \frac{\eta_i^2}{j\omega m_i + r_i + (k_i - k_{e,i})/(j\omega)} \\ &= G + jB. \end{aligned} \tag{37}$$

Based on the given geometry and modeling inputs, the modal parameters associated with the ECM at different in-plane vibration modes are reported in Table 2.

The modal mass factor $\chi_1 = 0.4876$ for the Lamé mode is found for our geometry very close to the classical $\chi_1^{sq} = 0.5000$ existing in the literature for the perfectly square membrane [40]. The difference is linked to the four tethers contribution on the total resonator surface. In the case of the butterfly and the extensional modes, their modal mass factors $\chi_2 = 0.2514$ and $\chi_3 = 0.8711$ differ a bit more from those obtained directly using the square plate mode shapes (*i.e.,* $\chi_2^{sq} = 0.2938$ and $\chi_3^{sq} = 0.7745$, respectively) and may lead to erroneous results if the problem geometry is not rigorously considered. The butterfly mode possesses the lowest modal mass factor in accordance with its smallest active surface (cf. Figure 2) while the extensional mode possesses the highest modal mass factor. In addition, the plate mode shape influence is also translated on the average modal electrostatic coefficient which varies depending on the considered bulk-mode. Note that the electrostatic coefficient value will change if one uses a different physical electrode coverage (cf. equation (22)).

In the FEM model, a multiphysics approach was taken, combining a structural mechanical analysis and an electrostatic analysis. The structural mechanical analysis was only applied for the resonator whose entire structure freely vibrates in air except for fixed constraints located on the sides of each T-shaped tether (cf. Figure 1). The material employed was anisotropic silicon whose tensor matrix is given in appendix A. The electrostatic analysis was applied to the whole setup where the resonator was electrically grounded and the electrode was excited with a 1 V harmonic perturbation. The setup was meshed using a fine, free triangular, physics-controlled mesh. A frequency domain study was set-up and performed using a two steps process, the stationary problem resolution followed by a frequency harmonic perturbation resolution. Confrontation between the lumped-element ECM and the FEM results is presented for each bulk-mode at different bias voltages on Figure 5.

From these results one sees that the lumped-element model and the FEM results are in excellent agreement. Resonances are located between 4 MHz and 5 MHz and the vibration amplitude coherently increases as the bias voltage increases. On the conductance, a clear resonance appear which is an ideal result to define clearly the quality factor and the resonance position of the system when it comes to experimental measurements. However, care must be taken with these simulations as the amplitude of the peaks is quite small and will be experimentally subjected to parasitic noises as well as stray impedances. Moreover, this ideal case does not consider ohmic losses and silicon piezoresistance hence the conductance is ideally null except at the resonance, which will likely be different in an experimental setup. As expected, because of the small electrode surface relative to the resonator surface, the bias voltage has no effect on the resonance position (*i.e.,* $k_{e,i} \ll k_i$).

The susceptance translates the capacitance of the device with a non-zero threshold value throughout the frequency spectrum. This result touches the frequently addressed problem of feedthrough capacitance in electrostatic MEMS resonator. This phenomenon deteriorates the resonance detection and reduces its dynamics [41]. Indeed, one sees that the amplitude threshold of the susceptance is much higher than the resonance amplitude itself. Hence, the introduction of even the smallest parasitic capacitance will effect these results and will impede the extraction of resonances values and quality factors from frequency magnitude curves or temporal signals. A practical solution commonly employed for the Lamé mode is to use differential amplifiers that enable feedthrough capacitance current canceling [42], [43].

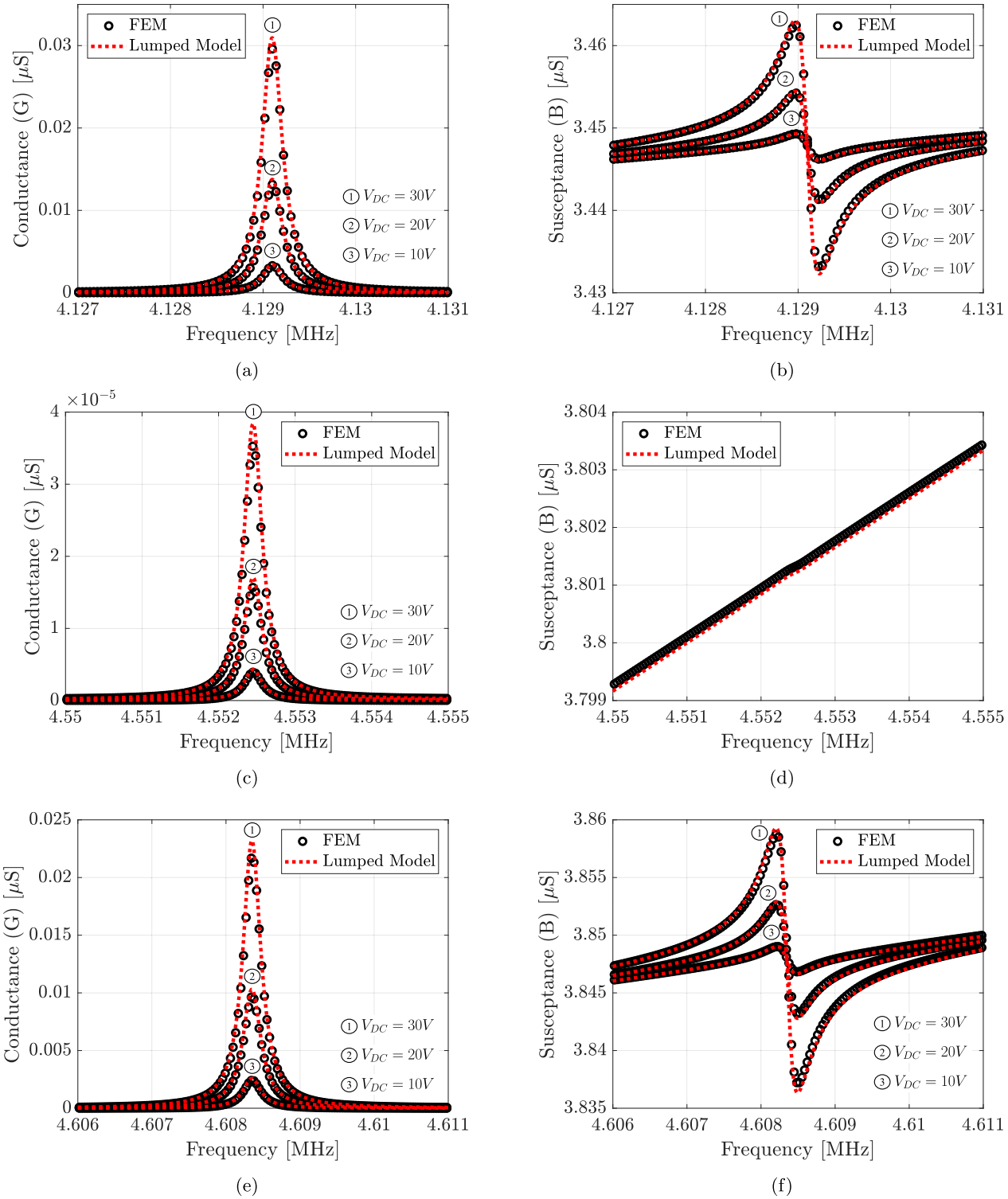

FIGURE 5. Electrical admittance simulation results comparison between FEM and the linear lumped-element equivalent circuit model in the case of: the Lamé vibration mode (a) conductance and (b) susceptance; the butterfly vibration mode (c) conductance and (d) susceptance; the extensional vibration mode (e) conductance and (f) susceptance. Each vibration mode is given for three different bias voltages except the butterfly mode susceptance result (d) where only the V_{DC} = 30 V is plotted because the curves for lower bias voltages are almost all identical.

We note that, in case of the butterfly mode, the resonance amplitudes are very small compared to the Lamé and extensional modes. The susceptance of the butterfly mode is plotted only for $V_{DC} = 30$ V because the curves for lower

bias voltages are almost all identical. Experimentally, this means that it is mandatory to separate the real and imaginary part of the result in order to accurately extract the intrinsic properties of the resonator from the plot. Alternatively, a fit algorithm could also be employed to obtain each individual parameter of the lumped-element equivalent circuit model introduced in this paper. Ultimately in this situation, the butterfly mode is not ideal for airborne particles detection due to its small active surface and small vibration amplitude.

V. DISCUSSIONS

The presented model combines a FEM eigenstudy with a modal analysis to create an ECM that provides major advantages: anisotropic materials can be employed; multilayered beams and plates of arbitrary geometry can be considered; equations can be resolved using simulation program with integrated circuit emphasis (SPICE); fast computation times are achieved. Indeed, the model combines the flexibility of FEM and the fastness of analytical equations computation. Note that, Gazzola et al. have also recently proposed a similar parameter-lumping approach oriented towards the design of piezoelectric micro-loudspeakers [44]. However, some drawbacks may impede its use depending on modeling requirements. To grasp the ultrasonic electrostatic MEMS modeling landscape and the relevance of the proposed approach, the advantages and drawbacks of existing techniques used to establish ECM are presented in Table 3.

A. LIMITATIONS

One intrinsic drawback of the presented model is the absence of nonlinearities from the simulation results, removed when performing a first-order Taylor expansion of the electrostatic force equation (17). The nonlinearities can be regrouped into two categories: first, the nonlinearities due to the additional stiffness and linked to a large displacement of the structure (*i.e.,* $\xi_i \not< h_{gap}$). These terms induce a frequency shift and produce results in the form of a Duffing equation with unstable regions translated by a frequency hysteresis behavior [49], [50]. These effects, known to be prominent in the case of electrostatic beams and cantilevers [51], [52], may be detrimental to accurately predict their behavior. In our case, the resonator is only clamped at each corner, laterally actuated over a small surface and a large gap which, by design, ensures that the additional stiffness is multiple orders of magnitude smaller than the resonator effective stiffness. This means that the small-displacement assumption is always true for non-aberrant actuation voltages. Second, the nonlinearities due to a large excitation voltage (*i.e.,* $V_{AC} \not< V_{DC}$). The electrostatic force produces a second-harmonic at twice the excited resonance frequency that may be of importance in the case of fluid-coupled MEMS (*e.g.,* nonlinear ultrasound imaging [53]). The presented model does not predict the second-harmonic but the latter does not affect the excited fundamental bulk-modes commonly used for air-coupled applications (*e.g.,* mass sensing).

Another intrinsic drawback of our method is the loss of membrane discretization when performing the modal analysis to obtain effective lumped-parameters and an analytical SPICE-compatible model. The FEM is employed for any desired geometry to obtain eigenvectors and eigenfrequencies before proceeding to a model order reduction. However, some may require the use of discretized problems for Green function computation in the case of fluid-coupled MEMS [54] or to apply concentrated loads [55] for example.

Additional limitations in the presented model are linked to phenomena that were voluntarily not addressed for clarity purposes, but can be added if desired to the model. For instance, residual stress from material deposition and oxide growth during microfabrication process may arise and affect MEMS performances (*e.g.,* frequency drift) [56]. Such phenomenon can be classically included directly in the mechanical behavioral equation (7) [9], [34], [57]. Moreover, the quality factor of the presented devices may also be affected by multiple phenomena that will decrease its overall sensitivity. For example, the presence of residual particles on the membrane, the anchors, the ambient temperature or material thermoelastic damping have all been shown to affect the mechanical damping of MEMS [58], [59], [60], [61]. The employed quality factors in this paper were arbitrarily fixed based on previous measurements but should be all individually studied to better understand the underlying physical damping mechanisms.

B. MASS SENSING APPLICATION CASE

This last section aims to exploit the developed model and analyze the behavior of the MEMS resonator subjected to a uniformly deposited mass. For that purpose, we consider a latex film whose Young modulus is equal to 2.8 MPa, Poisson coefficient to 0.33 and density 1050 kg/m^3 [62]. From an ECM perspective, the modified BVD circuit that accounts for a complex elastic loading of impedance Z_L is depicted Figure 6. In a practical case, this load corresponds to an additional mass and damping (*i.e.,* an additional inductance and resistance, respectively) that will cause the resonance properties to change. Here, we are only interested in the eigenfrequency shift linked to the additional mass.

Based on equation (12), the resonator resonance frequency becomes

$$f_i + \delta f_i = \frac{1}{2\pi}\sqrt{\frac{\{\phi_i\}^T[K]\{\phi_i\}}{\{\phi_i\}^T\left([M]+[M_L]\right)\{\phi_i\}}}\,, \tag{38}$$

where $[M_L]$ is the additional mass matrix and δf_i is the induced frequency shift at mode i.

For further analysis, the frequency shift can be written as a function of the total deposited mass m_L using a first-order Taylor expansion of equation (38). Classically referred to as the small-load assumption (SLA) [22], the deposited mass is assumed to be much smaller than the resonator effective mass (*i.e.,* $m_L \ll m_i$) and the resonance frequency shift much smaller than the resonance frequency

TABLE 3. Overview and comparison of existing ultrasonic electrostatic MEMS modeling techniques used to establish ECM. The loss of membrane discretization refers to the definition of equivalent electrical elements (*i.e.*, resistance, inductance, capacitance) contrary to more complex impedances classically obtained with discretized modeling techniques. SPICE compatibility refers to the ability of the ECM to be *directly* used as such for transient analyses.

Technique	Advantages	Drawbacks	Ref.
FEM (eigensolutions) + modal analysis	Fast computations ; Anisotropic materials ; Any structural geometry ; Multilayer structure ; SPICE-compatible.	Loss of membrane discretization ; Linear results.	This paper
Modal analysis	Instantaneous computations ; SPICE-compatible.	Presuppose mode-shapes knowledge ; Beam or plate assumptions ; Single layer isotropic-only material ; Loss of membrane discretization ; Linear results.	[25]–[27]
Deflection profile + beam or plate theory	Instantaneous computations ; SPICE-compatible ; Nonlinear results.	Presuppose deflection function knowledge ; Uniform pressure assumption ; Single layer isotropic-only material ; Loss of membrane discretization ; Beam or plate assumptions.	[45]–[47]
FEM	Nonlinear results ; Multilayer structure ; Anisotropic materials ; Any structural geometry ; Discretized membrane.	Heavy computations ; SPICE-incompatible.	[11], [33], [48]
Finite difference + beam or plate theory	Fast computations ; Multilayer structure ; Discretized membrane ; Some geometry flexibility.	Isotropic-only materials ; Beam or plate assumptions ; Linear results ; SPICE-incompatible.	[13], [34], [37]

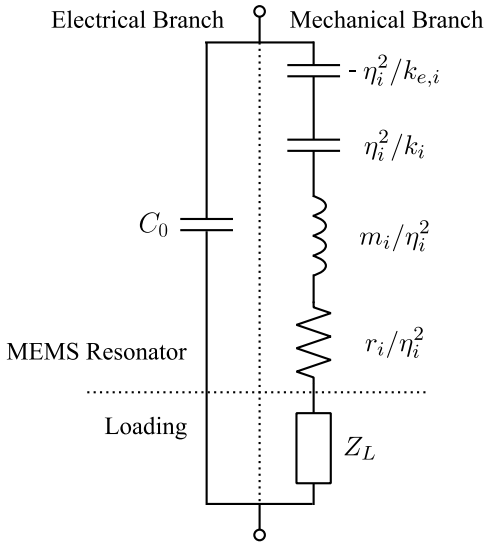

FIGURE 6. Butterworth-Van Dyke (BVD) equivalent circuit model of the loaded bulk-mode MEMS resonator. The mechanical branch loading is represented by a complex impedance denoted Z_L.

itself (*i.e.*, $\delta f_i \ll f_i$). This yields an expression analogous to the Sauerbrey equation such that

$$\delta f_i^{\mathrm{SLA}} = -\frac{f_i}{2m_i}\chi_i m_L \ , \tag{39}$$

where χ_i is the modal factor (cf. equation (10)) resulting from the combination of mode shape vectors. From the ECM perspective, this means the loading impedance Z_L corresponds to an additional inductance where

$$Z_L = \frac{j\omega\chi_i m_L}{\eta_i^2}. \tag{40}$$

This result must be taken with care because it does not consider the additional resistance value. Indeed, a separate analysis on the deposited material induced damping is required to precisely evaluate its influence on the resonator quality factor, which is out of the scope of this paper.

To evaluate the MEMS response and the SLA accuracy, the uniformly deposited mass thickness is progressively increased which, in turns, increases the total added mass. Figure 7 shows the frequency shift as a function of the deposited mass for the three bulk-modes obtained using the model based on equation (38) and compared with the SLA equation (39). Moreover, Table 4 summarizes the sensitivity computed in both cases. In the analytical linear SLA equation, the effective modal parameters (cf. Table 2) and mode shapes are assumed to not change as mass is progressively added.

Coherently, the frequency shift changes linearly with the deposited mass and each in-plane vibration mode possesses a different sensitivity. The difference between the model and the SLA equation progressively increases for multiple

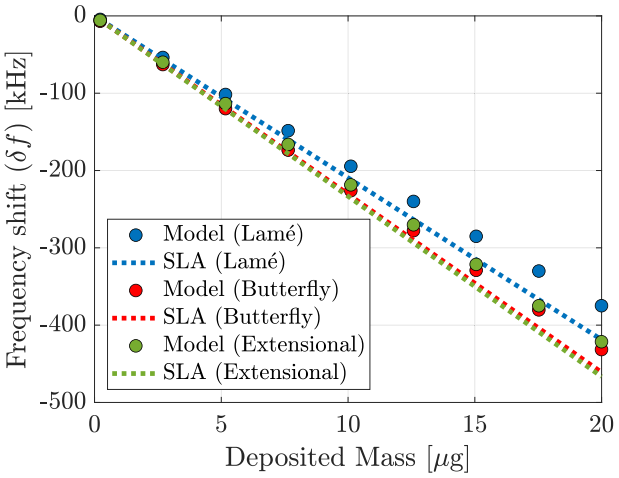

FIGURE 7. Frequency shift of the MEMS resonator as a function of the total deposited mass for the Lamé, butterfly and extensional in-plane vibration modes. Results displayed were obtained using the developed model and the SLA analytical equation (39).

TABLE 4. Comparison of the sensitivity (*i.e.*, $\delta f_i/m_L$) obtained using the model and directly with the small-load approximation (SLA) analytical equation (39).

Mode	Model (δf_i)	SLA ($\delta f_i^{\mathrm{SLA}}$)	Error
Lamé	−18.67 Hz/ng	−20.94 Hz/ng	12.2%
Butterfly	−21.40 Hz/ng	−23.05 Hz/ng	7.7%
Extensional	−21.09 Hz/ng	−23.33 Hz/ng	10.6%

reasons: the deposited mass progressively increases towards the effective resonator mass (*i.e.,* the SLA does not hold); the effective parameters such as k_i and χ_i are also slightly affected by the mass deposition (cf. the complex impedance Z_L Figure 6); the mode shapes changes with added mass. Interestingly, we observe different frequency shift values depending on the actuated vibration mode for the same deposited mass.

This application case demonstrate how the frequency shift of the resonator can be related to a deposited mass value. It also shows that the SLA approximation produces increasingly erroneous results as the added mass increases towards the resonator effective mass. Globally, the proposed model offers a better accuracy than the electrostatic MEMS adapted Sauerbrey equation.

VI. CONCLUSION

In this paper, a linear lumped-element equivalent circuit for ultrasonic air-coupled bulk-mode vibrating SCS MEMS with lateral electrostatic driving and capacitive sensing capabilities was introduced. The analytical equations dedicated to the eigenfrequencies prediction of a free anisotropic square body were proven to be an accurate representation of the behavior of a suspended square membrane anchored by T-shaped tethers. A modal analysis was performed to reduce the number of degrees of freedom of the discretized dynamic equation of motion and define lumped-parameters from a FEM eigenstudy. This process allows one to define different effective mass, stiffness and damping of the system for each individual vibration mode. Equivalent circuit representations were given based on the first order linearization of the electrostatic force and the current equation. The results led to the expression of the electrical static capacitance, the electro-mechanical transformation coefficients and the additional stiffness related to the membrane electrostatic actuation.

The lumped-element model electrical admittance results were confronted with a FEM analysis and displayed great accuracy with minimal computation time. The employed MEMS geometry depicts bulk-mode vibrations between 4 MHz and 5 MHz coherently with previous experimental measurements. As such, results showed that it is preferable to use the real part of the electrical admittance (*i.e.* the real part of the electrical current) to extract bulk-mode frequencies and quality factors of SCS MEMS resonators in an experimental setup. The duality between conductance and susceptance results demonstrates the importance of the driving electronics optimization when it comes to mass sensing applications.

In the broader landscape of ultrasonic electrostatic MEMS modeling, the presented model gathers the flexibility of FEM (*e.g.,* arbitrary geometry, multilayered anisotropic materials) and the practical aspect of analytical equations. If one is not limited by nonlinear effects and the loss of membrane discretization, this model becomes an ideal tool for MEMS resonator design and optimization. The relevance of the proposed MEMS topology and model was emphasized with a mass sensing numerical application. Indeed, the model provided more accurate results than the analogous expression to the Sauerbrey equation adapted for electrostatic MEMS. In addition, the resonator displayed a great sensitivity of more than 20 Hz/ng, ideal for small mass concentration sensing. With this model, an initial reference measurement and assuming that the deposited aerosol only adds mass and damping to the system, one will be able to relate airborne particles presence through precise ECM lumped-parameters variations.

From a modeling perspective, extension of this work involves nonlinear effects integration and capacitive fringing field consideration. Additional work is also required to incorporate the silicon piezoresistance influence, residual stress and mechanical damping mechanisms on the devices performance. Finally, optimization of the measurement chain through various amplifier architectures for real-time mass-sensing monitoring with SCS MEMS microbalances is currently undergoing experimental investigations.

APPENDIX A
ORTHOTROPIC SILICON TENSOR MATRIX

To define silicon properties, one must be mindful of the initial wafer position and crystal orientations. Indeed, the anisotropic nature of silicon causes the material to have different properties in each direction. Using the cubic symmetry of silicon, these "changing" properties are often described

using a 6 × 6 tensor matrix comprised of stiffness coefficients. As explained by Hopcroft et al. [30], silicon properties can also be describe using classical mechanical terms (*i.e.,* Young's modulus E_i and Poisson coefficients ν_{ij}) assuming orthotropic symmetry. In this case, the relationship between stress σ_{ij} and strain ε_{ij} in each direction (x, y, z) can be written as

$$\begin{bmatrix} \sigma_{xx} \\ \sigma_{yy} \\ \sigma_{zz} \\ \sigma_{yz} \\ \sigma_{zx} \\ \sigma_{xy} \end{bmatrix} = \begin{bmatrix} C_{11} & C_{12} & C_{13} & 0 & 0 & 0 \\ C_{12} & C_{22} & C_{23} & 0 & 0 & 0 \\ C_{13} & C_{23} & C_{33} & 0 & 0 & 0 \\ 0 & 0 & 0 & C_{44} & 0 & 0 \\ 0 & 0 & 0 & 0 & C_{55} & 0 \\ 0 & 0 & 0 & 0 & 0 & C_{66} \end{bmatrix} \begin{bmatrix} \varepsilon_{xx} \\ \varepsilon_{yy} \\ \varepsilon_{zz} \\ \varepsilon_{yz} \\ \varepsilon_{zx} \\ \varepsilon_{xy} \end{bmatrix}. \tag{41}$$

where C_{ij} are the tensor matrix terms.

In our case, we chose the normal of the wafer to be oriented towards the [100] direction and the other axes are aligned towards the ⟨110⟩ crystal directions. Hence, one gets $C_{11} = C_{22}$ and $C_{44} = C_{55}$. To compute the bulk-mode resonance frequencies in equations (1), (2) and (3), only the stiffness terms C_{11} and C_{12} are needed. These terms are equal to [30]

$$C_{11} = \frac{1 - \nu_{yz}\nu_{zy}}{E_y E_z \Delta}, \tag{42}$$

$$C_{12} = \frac{\nu_{yx} - \nu_{yz}\nu_{zy}}{E_y E_z \Delta}, \tag{43}$$

where

$$\Delta = \frac{1 - \nu_{xy}\nu_{yx} - \nu_{yz}\nu_{zy} - \nu_{zx}\nu_{xz} - 2\nu_{xy}\nu_{yz}\nu_{zx}}{E_x E_y E_z}. \tag{44}$$

Assuming a [110], [$\bar{1}$10], [001] silicon crystal orientation, the Young's modulus and Poisson coefficients in each directions are equal to

$$E_x = E_y = 169 \text{ GPa}, \tag{45}$$

$$E_z = 130 \text{ GPa}, \tag{46}$$

and

$$\nu_{yz} = \nu_{xz} = 0.36, \tag{47}$$

$$\nu_{zx} = \nu_{zy} = 0.28, \tag{48}$$

$$\nu_{xy} = \nu_{yx} = 0.064. \tag{49}$$

Note that the silicon anisotropy influences its mechanical behavior and should be taken into account to accurately model SCS MEMS.

APPENDIX B
SQUARE PLATE BULK-MODE SHAPES

The square plate mode shapes $[\phi]$ for bulk-mode vibrations are presented here based on H. Ekstein's work [29]. Because the problem is homogeneous, the amplitudes of the solutions are arbitrary and only the plate mode shapes are defined uniquely. As such, one may find arbitrary coefficients along these equations in the literature. He writes for the Lamé vibration mode along the x and y directions

$$[\phi_1^x] = \cos\left(\frac{\pi x}{L}\right)\sin\left(\frac{\pi y}{L}\right), \tag{50}$$

$$[\phi_1^y] = -\sin\left(\frac{\pi x}{L}\right)\cos\left(\frac{\pi y}{L}\right), \tag{51}$$

for the butterfly vibration mode

$$[\phi_2^x] = \left[\sin\left(\frac{\pi y}{L}\right) - \frac{\pi}{4}\right]\cos\left(\frac{\pi x}{L}\right), \tag{52}$$

$$[\phi_2^y] = \left[-\sin\left(\frac{\pi x}{L}\right) + \frac{\pi}{4}\right]\cos\left(\frac{\pi y}{L}\right), \tag{53}$$

and for the extensional vibration mode

$$[\phi_3^x] = \cos\left(\frac{\pi x}{L}\right), \tag{54}$$

$$[\phi_3^y] = \cos\left(\frac{\pi y}{L}\right). \tag{55}$$

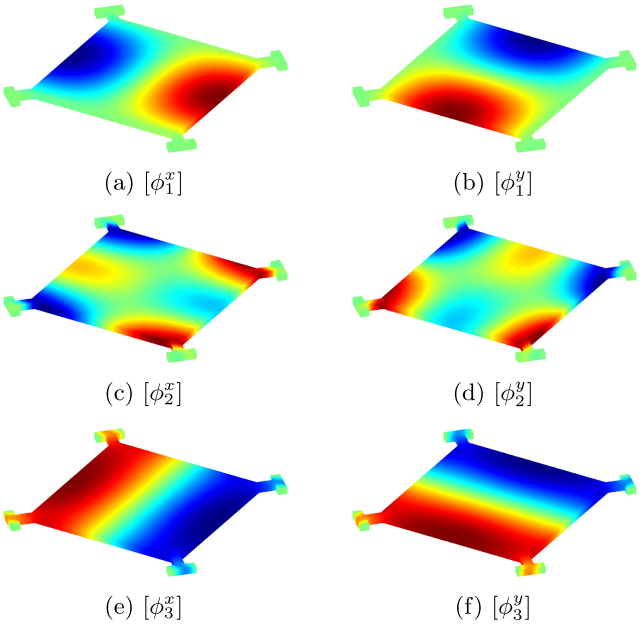

FIGURE 8. Plate mode shapes for the SCS MEMS with T-shaped tethers given for: the Lamé mode (a) along the *x* axis and (b) along the *y* axis; the butterfly mode (c) along the *x* axis and (d) along the *y* axis; the extensional mode (e) along the *x* axis and (f) along the *y* axis. The maximum plate displacement is depicted in red and the minimum in blue.

Using the MEMS geometry depicted Figure 1, an FEM analysis is performed to obtain the plate mode shapes in each directions and for each vibration mode. The results are presented Figure 8.

Interestingly, the FEM results for the plate with T-shaped tethers resembles that of the square plate mode shapes described by Ekstein's equations. As discussed in section IV, the Lamé mode is accurately depicted by these analytical equations while the butterfly and extensional plate mode shape equations should be used more cautiously to perform modal analysis and approximate the behavior of T-shaped tethered square plates.

ACKNOWLEDGMENT

This research was supported by the SATT ERGANEO in the framework of a maturation project dedicated to the design and fabrication of a micro-granulometer for aerosol measurement.

REFERENCES

[1] R. M. Langdon, "Resonator sensors—A review," *J. Phys. E, Sci. Instrum.*, vol. 18, no. 2, pp. 103–115, Feb. 1985.

[2] G. Stemme, "Resonant silicon sensors," *J. Micromech. Microeng.*, vol. 1, no. 2, pp. 113–125, Jun. 1991.

[3] H. A. C. Tilmans, M. Elwenspoek, and J. H. J. Fluitman, "Micro resonant force gauges," *Sens. Actuators A, Phys.*, vol. 30, nos. 1–2, pp. 35–53, Jan. 1992.

[4] M. Elwenspoek and R. Wiegerink, *Mechanical Microsensors* (Microtechnology and MEMS). Berlin, Germany: Springer, 2001.

[5] C. Nguyen, "MEMS technology for timing and frequency control," *IEEE Trans. Ultrason., Ferroelectr., Freq. Control*, vol. 54, no. 2, pp. 251–270, Feb. 2007.

[6] R. Abdolvand, B. Bahreyni, J. Lee, and F. Nabki, "Micromachined resonators: A review," *Micromachines*, vol. 7, no. 9, p. 160, Sep. 2016.

[7] G. Verma, K. Mondal, and A. Gupta, "Si-based MEMS resonant sensor: A review from microfabrication perspective," *Microelectron. J.*, vol. 118, Dec. 2021, Art. no. 105210.

[8] A. S. Algamili et al., "A review of actuation and sensing mechanisms in MEMS-based sensor devices," *Nanosc. Res. Lett.*, vol. 16, no. 1, p. 16, Jan. 2021.

[9] S. Timoshenko and S. Woinowsky-Krieger, *Theory of Plates and Shells*, 2nd ed. New York, NY, USA: McGraw-Hill, 1959.

[10] M. I. Younis, *MEMS Linear and Nonlinear Statics and Dynamics*, vol. 20. Boston, MA, USA: Springer, 2011.

[11] E. S. Hung and S. D. Senturia, "Generating efficient dynamical models for microelectromechanical systems from a few finite-element simulation runs," *J. Microelectromech. Syst.*, vol. 8, no. 3, pp. 280–289, 1999.

[12] A. H. Nayfeh, M. I. Younis, and E. M. Abdel-Rahman, "Reduced-order models for MEMS applications," *Nonlinear Dyn.*, vol. 41, nos. 1–3, pp. 211–236, Aug. 2005.

[13] T. Merrien, A. Boulmé, and D. Certon, "Lumped-parameter equivalent circuit modeling of CMUT array elements," *IEEE Open J. Ultrason., Ferroelectr., Freq. Control*, vol. 2, pp. 1–16, 2022.

[14] U. Soysal, E. Géhin, E. Algré, B. Berthelot, G. Da, and E. Robine, "Aerosol mass concentration measurements: Recent advancements of real-time nano/micro systems," *J. Aerosol Sci.*, vol. 114, pp. 42–54, Dec. 2017.

[15] J. E.-Y. Lee, Y. Zhu, and A. A. Seshia, "A bulk acoustic mode single-crystal silicon microresonator with a high-quality factor," *J. Micromech. Microeng.*, vol. 18, no. 6, Jun. 2008, Art. no. 064001.

[16] A. T.-H. Lin, J. E.-Y. Lee, J. Yan, and A. A. Seshia, "Methods for enhanced electrical transduction and characterization of micromechanical resonators," *Sens. Actuators A, Phys.*, vol. 158, no. 2, pp. 263–272, Mar. 2010.

[17] A. Prasad, J. Charmet, and A. A. Seshia, "Simultaneous interrogation of high-Q modes in a piezoelectric-on-silicon micromechanical resonator," *Sens. Actuators A, Phys.*, vol. 238, pp. 207–214, Feb. 2016.

[18] M.-H. Bao, "Electrostatic driving and capacitive sensing," in *Handbook of Sensors and Actuators*, vol. 8. Amsterdam, The Netherlands: Elsevier, 2000, pp. 139–198.

[19] U. Soysal, F. Marty, E. Géhin, C. Motzkus, and E. Algré, "Fabrication, electrical characterization and sub-Ng mass resolution of sub-μm air-gap bulk mode MEMS mass sensors for the detection of airborne particles," *Microelectron. Eng.*, vol. 221, Jan. 2020, Art. no. 111190.

[20] A. Hajjam, J. C. Wilson, and S. Pourkamali, "Individual air-borne particle mass measurement using high-frequency micromechanical resonators," *IEEE Sensors J.*, vol. 11, no. 11, pp. 2883–2890, Nov. 2011.

[21] U. Soysal, E. Géhin, F. Marty, E. Algré, E. Robine, and C. Motzkus, "Exploring deposition pattern characteristics of aerosols and bioaerosols by inertial impaction for the development of real-time silicon MEMS mass detection systems," *Aerosol Sci. Technol.*, vol. 55, no. 4, pp. 414–422, Apr. 2021.

[22] D. Johannsmann, *The Quartz Crystal Microbalance in Soft Matter Research: Fundamentals and Modeling*. Cham, Switzerland: Springer, 2015.

[23] F. D. Bannon, J. R. Clark, and C. T.-C. Nguyen, "High-Q HF microelectromechanical filters," *IEEE J. Solid-State Circuits*, vol. 35, no. 4, pp. 512–526, Apr. 2000.

[24] Y.-W. Lin, S. Lee, S.-S. Li, Y. Xie, Z. Ren, and C. T.-C. Nguyen, "Series-resonant VHF micromechanical resonator reference oscillators," *IEEE J. Solid-State Circuits*, vol. 39, no. 12, pp. 2477–2491, Dec. 2004.

[25] Z. Hao, S. Pourkamali, and F. Ayazi, "VHF single-crystal silicon elliptic bulk-mode capacitive disk resonators—Part I: Design and modeling," *J. Microelectromech. Syst.*, vol. 13, no. 6, pp. 1043–1053, Dec. 2004.

[26] H. A. C. Tilmans, "Equivalent circuit representation of electromechanical transducers: II. Distributed-parameter systems," *J. Micromech. Microeng.*, vol. 7, no. 4, pp. 285–309, Dec. 1997.

[27] M. Akgul, L. Wu, Z. Ren, and C. T.-C. Nguyen, "A negative-capacitance equivalent circuit model for parallel-plate capacitive-gap-transduced micromechanical resonators," *IEEE Trans. Ultrason., Ferroelectr., Freq. Control*, vol. 61, no. 5, pp. 849–869, May 2014.

[28] T. Singh et al., "Modeling of low-damping laterally actuated electrostatic MEMS," *Mechatronics*, vol. 52, pp. 1–6, Jun. 2018.

[29] H. Ekstein, "Free vibrations of anisotropic bodies," *Phys. Rev.*, vol. 66, nos. 5–6, pp. 108–118, Sep. 1944.

[30] M. A. Hopcroft, W. D. Nix, and T. W. Kenny, "What is the young's modulus of silicon?" *J. Microelectromech. Syst.*, vol. 19, no. 2, pp. 229–238, Apr. 2010.

[31] J. E.-Y. Lee, J. Yan, and A. A. Seshia, "Study of lateral mode SOI-MEMS resonators for reduced anchor loss," *J. Micromech. Microeng.*, vol. 21, no. 4, Apr. 2011, Art. no. 045010.

[32] Y. Xu and J. E.-Y. Lee, "Evidence on the impact of T-shaped tether variations on Q factor of bulk-mode square-plate resonators," in *Proc. 7th IEEE Int. Conf. Nano/Micro Engineered Mol. Syst. (NEMS)*, Mar. 2012, pp. 463–468.

[33] S. Satir, J. Zahorian, and F. L. Degertekin, "A large-signal model for CMUT arrays with arbitrary membrane geometry operating in non-collapsed mode," *IEEE Trans. Ultrason., Ferroelectr., Freq. Control*, vol. 60, no. 11, pp. 2426–2439, Nov. 2013.

[34] D. Certon, F. Teston, and F. Patat, "A finite difference model for cMUT devices," *IEEE Trans. Ultrason., Ferroelectr., Freq. Control*, vol. 52, no. 12, pp. 2199–2210, Dec. 2005.

[35] M. Liu and D. G. Gorman, "Formulation of Rayleigh damping and its extensions," *Comput. Struct.*, vol. 57, no. 2, pp. 277–285, Oct. 1995.

[36] A. Caronti, G. Caliano, A. Iula, and M. Pappalardo, "An accurate model for capacitive micromachined ultrasonic transducers," *IEEE Trans. Ultrason., Ferroelectr., Freq. Control*, vol. 49, no. 2, pp. 159–168, Feb. 2002.

[37] A. Boulmé and D. Certon, "Design of broadband linear micromachined ultrasonic transducer arrays by means of boundary element method coupled with normal mode theory," *IEEE Trans. Ultrason., Ferroelectr., Freq. Control*, vol. 62, no. 9, pp. 1704–1716, Sep. 2015.

[38] S. P. Mao et al., "Modal analysis based equivalent circuit model and its verification for a single cMUT cell," *J. Micromech. Microeng.*, vol. 27, no. 3, Mar. 2017, Art. no. 035001.

[39] A. Cagliani and Z. J. Davis, "Bulk disk resonator based ultrasensitive mass sensor," in *Proc. IEEE Sensors*, Oct. 2009, pp. 1317–1320.

[40] J. E.-Y. Lee, "Lamé mode MEMS resonators," in *Encyclopedia of Nanotechnology*, B. Bhushan, Ed. Dordrecht, The Netherlands: Springer, 2015, pp. 1–9.

[41] J. E.-Y. Lee and A. A. Seshia, "Direct parameter extraction in feedthrough-embedded capacitive MEMS resonators," *Sens. Actuators A, Phys.*, vol. 167, no. 2, pp. 237–244, Jun. 2011.

[42] M. Kangül, E. Aydin, F. Gökçe, Ö. Zorlu, and H. Külah, "Analysis and elimination of the capacitive feedthrough current on electrostatically actuated and sensed resonance-based MEMS sensors," *J. Microelectromech. Syst.*, vol. 26, no. 6, pp. 1272–1278, Dec. 2017.

[43] Y. Wu, C. Fan, L. Gu, M. Liu, X. Wu, and F. Cui, "Feedthrough effect in MEMS gyroscopes and fully differential feedthrough cancellation method," *Rev. Sci. Instrum.*, vol. 95, no. 1, Jan. 2024, Art. no. 015001.

[44] C. Gazzola, V. Zega, A. Corigliano, P. Lotton, and M. Melon, "A reduced-order-model-based equivalent circuit for piezoelectric micro-electro-mechanical-system loudspeakers modeling," *J. Acoust. Soc. Amer.*, vol. 155, no. 2, pp. 1503–1514, Feb. 2024.

[45] H. Koymen et al., "An improved lumped element nonlinear circuit model for a circular CMUT cell," *IEEE Trans. Ultrason., Ferroelectr., Freq. Control*, vol. 59, no. 8, pp. 1791–1799, Aug. 2012.

[46] M. Maadi and R. J. Zemp, "A nonlinear lumped equivalent circuit model for a single uncollapsed square CMUT cell," *IEEE Trans. Ultrason., Ferroelectr., Freq. Control*, vol. 66, no. 8, pp. 1340–1351, Aug. 2019.
[47] I. O. Wygant, M. Kupnik, and B. T. Khuri-Yakub, "An analytical model for capacitive pressure transducers with circular geometry," *J. Microelectromech. Syst.*, vol. 27, no. 3, pp. 448–456, Jun. 2018.
[48] G. G. Yaralioglu, S. A. Ergun, and B. T. Khuri-Yakub, "Finite-element analysis of capacitive micromachined ultrasonic transducers," *IEEE Trans. Ultrason., Ferroelectr., Freq. Control*, vol. 52, no. 12, pp. 2185–2198, Dec. 2005.
[49] R. Lifshitz and M. C. Cross, "Nonlinear dynamics of nanomechanical and micromechanical resonators," in *Reviews of Nonlinear Dynamics and Complexity*, 1st ed., H. G. Schuster, Ed. Hoboken, NJ, USA: Wiley, 2008, pp. 1–52.
[50] A. Z. Hajjaj, N. Jaber, S. Ilyas, F. K. Alfosail, and M. I. Younis, "Linear and nonlinear dynamics of micro and nano-resonators: Review of recent advances," *Int. J. Non-Linear Mech.*, vol. 119, Mar. 2020, Art. no. 103328.
[51] R. M. C. Mestrom, R. H. B. Fey, J. T. M. van Beek, K. L. Phan, and H. Nijmeijer, "Modelling the dynamics of a MEMS resonator: Simulations and experiments," *Sens. Actuators A, Phys.*, vol. 142, no. 1, pp. 306–315, Mar. 2008.
[52] M. H. Ghayesh, H. Farokhi, and M. Amabili, "Nonlinear behaviour of electrically actuated MEMS resonators," *Int. J. Eng. Sci.*, vol. 71, pp. 137–155, Oct. 2013.
[53] A. Novell, M. Legros, N. Felix, and A. Bouakaz, "Exploitation of capacitive micromachined transducers for nonlinear ultrasound imaging," *IEEE Trans. Ultrason., Ferroelectr., Freq. Control*, vol. 56, no. 12, pp. 2733–2743, Dec. 2009.
[54] V. Goepfert, A. Boulmé, F. Levassort, T. Merrien, R. Rouffaud, and D. Certon, "Modeling a fluid-coupled single piezoelectric micromachined ultrasonic transducer using the finite difference method," *Micromachines*, vol. 14, no. 11, p. 2089, Nov. 2023.
[55] K. Li, W. Chen, W. Zhang, and G. Ma, "Electromechanical coupling analysis for MEMS featured by stepped-height structure and concentrated load," *Microsyst. Technol.*, vol. 15, no. 4, pp. 621–635, Apr. 2009.
[56] S. Dutta and A. Pandey, "Overview of residual stress in MEMS structures: Its origin, measurement, and control," *J. Mater. Sci., Mater. Electron.*, vol. 32, no. 6, pp. 6705–6741, Mar. 2021.
[57] M. Engholm, T. Pedersen, and E. V. Thomsen, "Modeling of plates with multiple anisotropic layers and residual stress," *Sens. Actuators A, Phys.*, vol. 240, pp. 70–79, Apr. 2016.
[58] S. Ghaffari et al., "Accurate modeling of quality factor behavior of complex silicon MEMS resonators," *J. Microelectromech. Syst.*, vol. 24, no. 2, pp. 276–288, Apr. 2015.
[59] Z. Chen et al., "A novel Lamé mode RF-MEMS resonator with high quality factor," *Int. J. Mech. Sci.*, vol. 204, Aug. 2021, Art. no. 106484.
[60] T. Feng, Q. Yuan, D. Yu, B. Wu, and H. Wang, "Concepts and key technologies of microelectromechanical systems resonators," *Micromachines*, vol. 13, no. 12, p. 2195, Dec. 2022.
[61] A.-R. Kolahdouz-Moghaddam, S. Nabavi, and F. Nabki, "Temperature dependence modeling and thermal sensitivity reduction of bulk micromachined silicon MEMS Lamé resonators," *J. Microelectromech. Syst.*, vol. 32, no. 4, pp. 314–326, Aug. 2023.
[62] C.-J. Tsai, D. Y. H. Pui, and B. Y. H. Liu, "Elastic flattening and particle adhesion," *Aerosol Sci. Technol.*, vol. 15, no. 4, pp. 239–255, Jan. 1991.

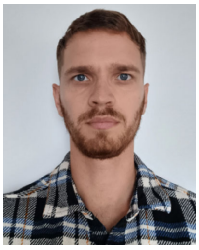

TONY MERRIEN was born in Rennes, France, in 1994. He received the M.Sc. degree in acoustics from École Centrale de Lyon, France, in 2018, and the Ph.D. degree in electronics from the University of Tours, France, in 2022. His Ph.D. thesis was dedicated to the development of capacitive micromachined ultrasonic transducers (CMUT) for 3D imaging. In 2023, he joined the ESYCOM Laboratory, Noisy-le-Grand, France, as a Research Engineer. His current research interests include micro-electro-mechanical systems (MEMS) modeling, characterization, optimization, and integration for air quality monitoring.

PIERRE DIDIER received the M.Eng. degree from Paris XIII University, France, in 2013, and the Ph.D. degree from ENS Paris-Saclay, France, under the direction of Prof. Larzabal, in 2017. From 2018 to 2020, he was with the LIMMS Laboratory and the Minami Laboratory, The University of Tokyo, Japan, as a JSPS Post-Doctoral Fellow. Since 2020, he has been an Associate Professor with Université Paris-Est Créteil (UPEC), France. His research interests include biosensors, instrumentation, and micro-devices dedicated to indoor air quality.

EMMANUELLE ALGRÉ received the master's degree in physics, nanostructures and materials and the Engineering degree in material physics from ENSPG-INPG, Grenoble, France. From 2007 to 2009, she was a Post-Doctoral Fellow with the Nano and Microsystem Group, Institut d'Électronique, de Microélectronique et de Nanotechnologie (IEMN), Villeneuve-d'Ascq, France, on the development of MEMS silicon ring resonator for high sensitive atomic force microscope probe. She realized a thesis in the Spintronique et Technologie des Composants (SPINTEC) Laboratory, Grenoble, on the development of near-field thermomagnetic recording for ultra-high capacity storage on hard disk. In 2006, she had a thesis in material physics from Joseph Fourier University, Grenoble. She is currently an Associate Professor with ESIEE and a Researcher on sensor and nanotechnology with the ESYCOM Laboratory, Noisy-le-Grand, France. She has developed expertise for more than 15 years in MEMS technologies and micro and nanofabrication technologies, in particular for air quality measurement. She is also leading a project supported by the SATT ERGANEO dedicated to the development of microsized aerosol granulometer devices.